Robust flow of light in three-dimensional dielectric photonic crystals

Wen-Jie Chen,[1] Shao-Ji Jiang,[1,2] and Jian-Wen Dong[1,*]

[1]*State Key Laboratory of Optoelectronic Materials and Technologies, Sun Yat-Sen University, Guangzhou 510275, China*

[2]*e-mail: stsjsj@mail.sysu.edu.cn*

**Corresponding author: dongjwen@mail.sysu.edu.cn*

Received June 17, 2013; revised August 6, 2013; accepted August 7, 2013;
posted August 9, 2013 (Doc. ID 192466); published August 30, 2013

Chiral defect waveguides and waveguide bend geometry were designed in diamond photonic crystal to mold the flow of light in three dimensions. Propagations of electromagnetic waves in chiral waveguides are robust against isotropic obstacles, which would suppress backscattering in waveguides or integrated devices. Finite-difference time-domain simulations demonstrate that high coupling efficiency through the bend corner is preserved in the polarization gap, as it provides an additional constraint on the polarization state of the backscattered wave. Transport robustness is also demonstrated by inserting two metallic slabs into the waveguide bend. © 2013 Optical Society of America

OCIS codes: (160.5298) Photonic crystals; (160.1585) Chiral media; (230.7380) Waveguides, channeled.
http://dx.doi.org/10.1364/OL.38.003460

Robust transport refers to the insusceptibility of an electron's propagation to impurity or disorder, which is a distinguishing feature of topological states (chiral edge states of quantum Hall insulators [1,2] and helical edge states of quantum spin Hall insulators [3]). As the concepts of electronic topological states were mapped to the photonic system [4–13] in the past few years, researchers found that edge states of certain types of photonic crystals (PhCs) have robust transport properties similar to electrons. Light scattering loss and attenuation in either waveguides or integrated devices, which are attributed to the fabrication error or deformation of devices, limit optical communication distance and the efficiency of devices. Therefore, the robust transport properties of electromagnetic waves have great significance in the era of optical communication, for their capability to suppress light backscattering or attenuation in optical circuits.

Two types of robust transports based on topological bands of PhCs have been proposed and investigated. One relies on one-way transport of light at the edge of photonic quantum Hall insulators [4–12]. By applying an external magnetic field on two-dimensional (2D) magnetic PhCs, photonic bands of the time-reversal broken system acquire nonzero Chern numbers, and thus one-way edge states appear in the topologically nontrivial bandgap. The propagation of light is robust against backscattering from obstacles due to the lack of a backward propagating mode. The other type of robust transport based on topological bands was proposed very recently along with photonic quantum spin Hall insulators [13]. The magneto-electric coupling effect of 2D bianisotropic PhCs composed of conceptual metamaterials emulates the spin-orbit coupling of electrons. The corresponding photonic bands of the time-reversal invariant system acquire nonzero spin Chern numbers. Gapless spin-polarized edge states also appear in the topologically nontrivial bandgap. The propagation of light can be also backscattering-immune for the decoupling between forward edge states and backward edge states. However, both types mentioned above are hardly to be extended to the optical communication regime, for the reason of the weak gyrotropic effect of magnetic materials and strong loss-dispersive metamaterials, respectively. Another issue is that the flows of light in the above two methods are usually restricted in the 2D plane, because backscattering immunity disappears in the third dimension. Similar topologically protected transport can also be achieved in the microwave regime via 2D networks of metamaterial elements [14]. Photonic Floquet topological insulators [15] were proposed to realize robust edge states for visible light, but 10 cm long waveguide arrays are required.

For these reasons, we proposed another type of robust transport mechanism [16], which can be realized in the topologically trivial bandgap of dielectric layer-by-layer PhCs. It is based on chirality of guided modes in the waveguides with chiral geometry. The helical symmetry of the chiral waveguide lifts off the degeneracy between left-handed (LH) and right-handed (RH) waveguide modes, and opens a polarization gap that allows only one particular circularly polarized wave to propagate. Reflection from an isotropic scatterer would change the handedness of guided waves in the chiral waveguide, but propagation of the opposite handedness wave is forbidden in the polarization gap. Consequently, the flow of light is robust (but still two-way) against backscattering from an isotropic obstacle. This mechanism requires neither time-reversal breaking nor magnetic materials and bianisotropic metamaterials. This is similar to the fact that electronic transport in topological insulators is robust only when the impurity is nonmagnetic, although the gap topology is completely different. As the PhC is composed of all dielectrics, it can be scaled into all frequency ranges, as well as the optical communication regime. In addition, the layer-by-layer geometry of the PhC has the natural advantage that it can control the flow of light in all three dimensions.

In this Letter, we designed a chiral defect waveguide and a waveguide bend geometry in diamond PhCs. The motivation is to design a bend channel in which the energy will not be reflected even if the isotropic obstacle

is introduced, so as to achieve robust flow of light in three dimensions. Transmission spectra through the waveguide bend and a straight waveguide were studied. We found that the coupling efficiency in the polarization gap was intensively preserved by the backscattering suppression effect. Robustness against isotropic obstacles was also demonstrated in the bend waveguide.

We choose diamond PhC to construct a three-dimensional waveguide network because diamond lattice has the largest complete bandgap and three symmetrical crystal orientations [(100), (010), and (001)]. Thus, chiral waveguides along these directions can have the same geometry and dispersion relation in order to attain a broader working bandwidth.

A chiral defect waveguide in PhCs can be constructed by removing or infiltrating dielectric materials surrounding the spiral axis. Figure 1(a) depicts a spiral with LH geometry along the z direction [(001) crystal orientation] by connecting lattice points [17]. Figure 1(b) shows the morphology of a chiral defect in a diamond PhC, by removing an LH spiral [Fig. 1(c)]. In our simulations, the diamond PhC, whose lattice constant is assumed to be a, is made up of dielectric material with a refractive index of 3.6 and air background. The size of the chiral defect is $0.424a \times 0.424a$. The corresponding dispersion relation was calculated by the plane wave expansion method [18], as shown in Fig. 1(e). The upper and lower gray regions correspond to the passing bands, between which is a complete bandgap. There are four handed nondegeneracy defect modes in the complete gap, two of which are LH polarized, and the others are RH polarized. Here, LH and RH polarizations indicate that the electric field vectors of the defect modes form LH and RH helices along the propagation direction at a fixed instant of time. The most important is that an RH polarization gap with a relative bandwidth of 5.9% opens up at Γ point from the normalized frequency 0.478 to $0.507(c/a)$, where robust transport occurs [16]. To give an overview on the eigenfield distribution of the defect mode, an iso-amplitude surface (red) of the magnetic field is plotted in Fig. 1(d),

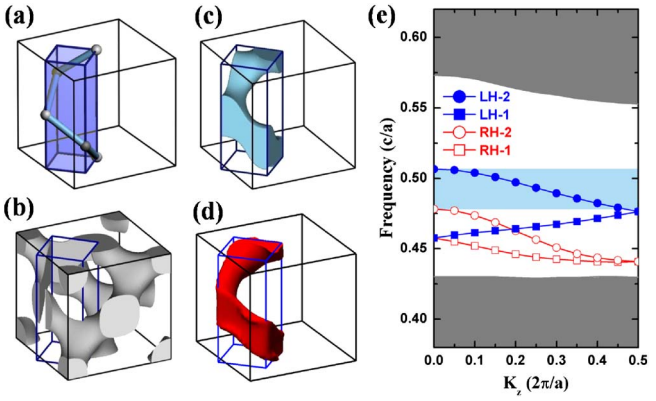

Fig. 1. Schematic of the chiral waveguide and the dispersion relation. (a) An LH spiral formed by connecting lattice points in diamond lattices. The black frame represents a cubic unit cell. (b) LH chiral defect by removing the LH spiral in diamond PhC. The blue frame denotes the edges of the chiral defect. (c) Segment removed from diamond PhC. (d) Iso-amplitude surface of magnetic field for the LH waveguide mode at $0.49(c/a)$. (e) Dispersion relation of LH waveguide along the z direction in diamond PhC.

for the LH defect mode at a frequency of $0.49(c/a)$. It can be seen that the magnetic fields are mainly localized around the missing spiral. In the same way, the LH defect waveguides along the x and y directions can also be constructed, and the dispersion relations are identical to those of Fig. 1(e). It is notable that the dispersion relation of the RH defect waveguide is alike, except that the polarization characteristics are reversed.

Next we will design the bend geometry of the chiral waveguide in order to obtain a high coupling coefficient. Without loss of generality, we only discuss the coupling between waveguides along the z and x directions. There are two kinds of bends depending on whether two chiral waveguides have the same handedness. Suppose that the z direction waveguides in both cases are LH. Figure 2 shows the schematic diagram near the corner in lattice form. Gray spheres represent the lattice points of the missing spirals, and the light blue (red) columns connecting them are the spirals' arms. Blue (red) square tubes outline the defect boundaries, inside which is vacuum. The LH circularly polarized wave is incident from the bottom and couples into the LH chiral waveguide along the z direction. And then the guided wave is coupled to another LH/RH waveguide through the corner. We will discuss the coupling efficiencies when the transmitted waveguide in the x direction is LH or RH.

The coupling efficiency between two guided modes is closely related to the spatial distributions, polarization directions, and temporal evolutions of the eigenmodes. Once these features of two modes match well, the coupling between them should be strong. As has been mentioned in [16], fields of the defect modes in the polarization gap are localized around the missing spiral and the circular polarization has the same handedness with defect. Consider the case in which the transmitted waveguide is LH, which is represented by a horizontal blue tube in Fig. 2(a). The yellow cylinder highlights the overlapped region of the vertical and horizontal missing spirals, where modes' coupling may occur. However, the polarization states of both modes do not match in the overlapped region. Black circular arrows near the waveguide entrance and exit denote two waveguide modes' polarization planes and rotational directions of

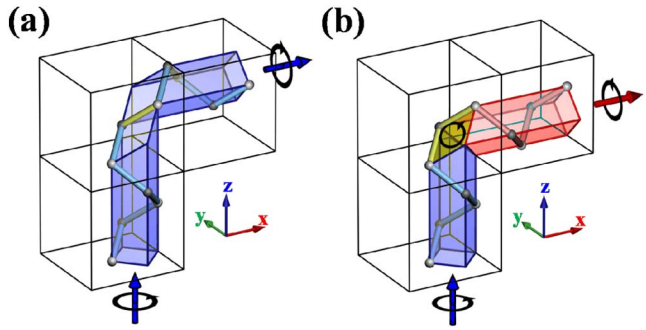

Fig. 2. Two schematic diagrams for bends between waveguides in the z and x directions. (a) WGZ-WGX (L2L): LH waveguides in both directions. (b) WGZ-WGX (L2R): LH waveguide in the z direction and RH waveguide in the x direction. Three cubic cells are shown in both figures. Each arrow near the entrance/exit denotes either the incident or the transmitted wave, and the circular arrow around it denotes the rotational direction of electromagnetic fields.

electric fields. The electric field of the vertical mode is polarized in the xy plane and rotates counterclockwise, while the electric field of the horizontal mode is polarized in the yz plane. As a result, the coupling efficiency between two LH waveguides would be relatively low.

Then we consider the other case in which the transmitted waveguide has opposite handedness to the incident waveguide; see Fig. 2(b). The RH transmitted waveguide is represented by a horizontal red tube. We find that the vertical and horizontal waveguides have two spiral arms in common (highlighted by yellow cylinders). This indicates that coupling should be stronger than the bend geometry in Fig. 2(a), which has only one common spiral arm. It is notable that the handedness of the circularly polarized wave propagating in the vertical and horizontal waveguides is opposite. The electric field of the vertical mode rotates counterclockwise in the xy plane, while that of the horizontal mode rotates clockwise in the yz plane. To satisfy the conservation of the tangential electric/magnetic field at the boundaries of the bend corner, we can simply set the corner boundary to be a 45° oblique plane; see the yellow rhombus in Fig. 2(b). In this way, the tangential electric fields of both modes projected onto this plane (elliptic arrow) can be conserved. The oblique plane serves as a reflective mirror that reflects the incident LH wave propagating along the z direction into an RH wave propagating along the x direction. Since the spatial distributions and tangential electric/magnetic fields match well between two waveguide modes, high transmittance through this waveguide bend is expected.

In order to demonstrate the idea, we calculated the transmission spectra through two bend waveguides proposed in Fig. 2 using the finite-difference time-domain method [19]. The diamond PhC with a size of $10a \times 10a \times 10a$ was simulated, at the center of which a 10a-long LH straight waveguide was located. An ex-polarized source placed $1a$ below the waveguide entrance, emitting a Gaussian pulse with a center frequency of $0.48(c/a)$ and a pulsewidth of $0.4(c/a)$. The detector at $1a$ above the waveguide exit received the transmitted wave. Configurations for simulating the waveguide bend are the same, except the waveguide geometry and the position of the detector.

The transmission spectra for bend waveguides are plotted in Figs. 3(a) and 3(b) by red curves. Transmission spectra for a straight waveguide along the z direction are also shown by black curves for reference. Figure 3(a) shows the transmission spectrum for the bend waveguide of Fig. 2(a), where both incident and transmitted waveguides are LH. The transmission in the polarization gap (highlighted by the light blue box) drops a lot in comparison with the straight waveguide. On the other hand, the transmission for the bend waveguide in Fig. 2(b) is shown in Fig. 3(b). We can see that the transmissions for the bend waveguide and the straight waveguide are almost the same in the polarization gap, which verifies the strong coupling between the LH vertical mode and the RH horizontal mode. It can be inferred that the coupling between them should also be strong outside the polarization gap. So is the coupling between the RH vertical mode and the LH horizontal mode, as their spatial distributions and tangential electric/magnetic fields match well. The ex-polarized source excites both LH and RH

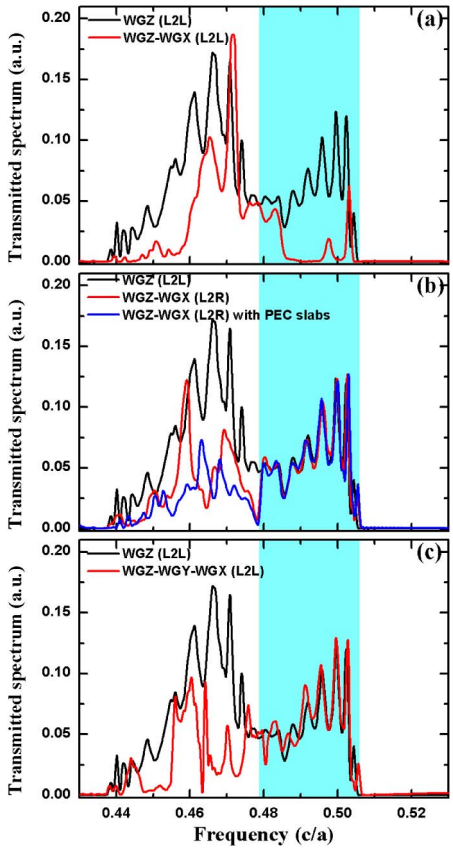

Fig. 3. Transmission spectra (red) for three types of bend waveguides: (a) WGZ-WGX (L2L) shown in Fig. 2(a), (b) WGZ-WGX (L2R) shown in Fig. 2(b), and (c) double-bend waveguide WGZ-WGY-WGX (L2L). The transmission spectra for the straight waveguide WGZ (L2L) are also plotted (black). Here, L2L means both the input and output waveguides are LH. L2R means that the input and output waveguides are LH and RH, respectively. The light blue box highlights the polarization gap. The blue line in (b) refers to WGZ-WGX (L2R) with two PEC obstacles inside.

vertical modes in this frequency region, and then these two modes couple to the RH and LH horizontal modes, respectively. Therefore, transmission through the bend waveguide of Fig. 2(b) seemingly should equal the one through the straight waveguide. But the bend transmission outside the polarization gap is not as high as straight waveguide, a fact that is in contrast to the case inside the gap. The reason is that the LH (RH) upward vertical mode can also couple to RH (LH) downward mode at the bend corner, as both of their electric/magnetic fields rotate counterclockwise (clockwise). On the other hand, the high bend efficiency in the polarization gap is due to not only the strong coupling between the LH vertical mode and the RH horizontal mode, but also the backscattering suppression effect, because field vectors of the upward mode and the downward mode always rotate in opposite directions.

Figure 4 depicts the amplitude profile of energy flow for the bend waveguide in the xz plane, in which a continuous ex-source with a frequency of $0.49(c/a)$ is $1a$ beneath the waveguide entrance. Figures 4(a) and 4(b) correspond to the bend geometries in Figs. 2(a) and 2(b), respectively. For the first-type of bend, the energy flow in

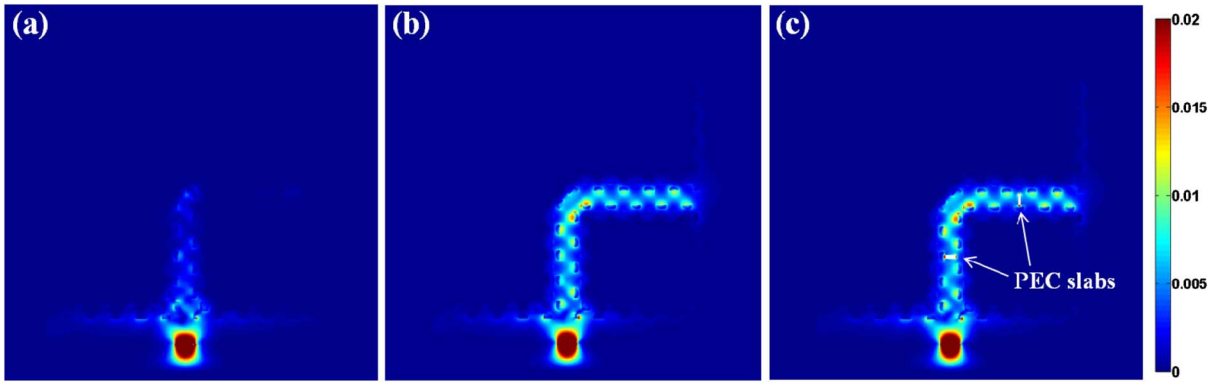

Fig. 4. Amplitude profile of energy flow for two types of single bend waveguides in the xz plane at the frequency of $0.49(c/a)$: (a) and (b) are for the bend geometries in Figs. 2(a) and 2(b), while (c) is the same as (b) but with two PEC slabs inside.

the z direction waveguide is relatively small, as most of the LH wave is reflected by bend corner. The energy flow of the upward LH wave cancels out with the reflected wave. However, no obvious backscattering can be observed for the second-type of bend; see Fig. 4(b).

To confirm the transport robustness against the isotropic scatterer, two perfect electronic conductor (PEC) slabs with size of $0.3a \times 0.3a \times 0.1a$ are inserted into the bend waveguide in Fig. 4(b). One slab locates at the center of the vertical waveguide, and the other is in the horizontal waveguide. The simulated energy flow is shown in Fig. 4(c). The energy flow is almost the same as in Fig. 4(b), except that it evades the PEC slabs. This indicates that no obvious backscattering is introduced by the isotropic obstacles. This is also confirmed by the calculated transmission spectrum; see the blue line in Fig. 3(b).

Note that the waveguide bend in Fig. 2(b) can reverse the polarization state of the guided wave, as the guided wave in the transmitted waveguide is RH polarized rather than LH polarized. This may bring about problems when connecting two circuits of the same handedness. This can be solved in a simple way. It seems that the LH chiral waveguide along the z direction cannot couple directly to another LH waveguide along the x direction. But the LH waveguide in the z direction can still couple to another one in the x direction through two bends: the waves first couple to the RH waveguide in the y direction and then to another LH waveguide in the x direction. The transmitted spectrum for this double-bend waveguide is illustrated in Fig. 3(c) by a red line, and high transmission is also preserved in the polarization gap as expected.

In conclusion, we designed a chiral defect waveguide and waveguide bend geometry in diamond PhCs. We achieved a polarization gap of defect modes with a relative bandwidth of 5.9% where robust transport occurs. Transmission spectra through the bend waveguide and a straight waveguide were compared to demonstrate bend efficiency, and we found that the coupling coefficient in the polarization gap was intensively preserved by the backscattering suppression effect.

This work is supported by the National Natural Science Foundation of China (11274396, 11074311), the National 973 project (2014CB931700), the grant for Guangdong Distinguished Young Scientists. JWD is also supported by the FRFCU (2012300003162498), the GDNSF (S2012010010537), and the Fund of OEMT.

References

1. K. von Klitzing, G. Dorda, and M. Pepper, Phys. Rev. Lett. **45**, 494 (1980).
2. F. D. M. Haldane, Phys. Rev. Lett. **61**, 2015 (1988).
3. C. L. Kane and E. J. Mele, Phys. Rev. Lett. **95**, 226801 (2005).
4. F. D. M. Haldane and S. Raghu, Phys. Rev. Lett. **100**, 013904 (2008).
5. S. Raghu and F. D. M. Haldane, Phys. Rev. A **78**, 033834 (2008).
6. Z. Wang, Y. D. Chong, J. D. Joannopoulos, and M. Soljačić, Phys. Rev. Lett. **100**, 013905 (2008).
7. Z. Wang, Y. D. Chong, J. D. Joannopoulos, and M. Soljačić, Nature **461**, 772 (2009).
8. X. Ao, Z. F. Lin, and C. T. Chan, Phys. Rev. B **80**, 033105 (2009).
9. Y. Poo, R.-X. Wu, Z. F. Lin, Y. Yang, and C. T. Chan, Phys. Rev. Lett. **106**, 093903 (2011).
10. T. Ochiai and M. Onoda, Phys. Rev. B **80**, 155103 (2009).
11. J.-X. Fu, R.-J. Liu, and Z.-Y. Li, Appl. Phys. Lett. **97**, 041112 (2010).
12. C. He, X.-L. Chen, M.-H. Lu, X.-F. Li, W.-W. Wan, X.-S. Qian, R.-C. Yin, and Y.-F. Chen, Appl. Phys. Lett. **96**, 111111 (2010).
13. A. B. Khanikaev, S. H. Mousavi, W.-K. Tse, M. Kargarian, A. H. MacDonald, and G. Shvets, Nat. Mater. **12**, 233 (2012).
14. V. Yannopapas, New J. Phys. **14**, 113017 (2012).
15. M. C. Rechtsman, J. M. Zeuner, Y. Plotnik, Y. Lumer, D. Podolsky, F. Dreisow, S. Nolte, M. Segev, and A. Szameit, Nature **496**, 196 (2013).
16. W.-J. Chen, Z. H. Hang, J.-W. Dong, X. Xiao, H.-Z. Wang, and C. T. Chan, Phys. Rev. Lett. **107**, 023901 (2011).
17. A. Chutinan and S. Noda, Phys. Rev. B **57**, R2006 (1998).
18. http://ab-initio.mit.edu/wiki/index.php/MIT_Photonic_Bands.
19. A. F. Oskool, D. Roundy, M. Ibanescu, P. Bermei, J. D. Joannopoulos, and S. G. Johnson, Comput. Phys. Commun. **181**, 687 (2010).